INTERNATIONAL JOURNAL FOR NUMERICAL METHODS IN FLUIDS
Int. J. Numer. Meth. Fluids 2003; **43**:1019–1044 (DOI: 10.1002/fld.510)

URANS computations for an oscillatory non-isothermal triple-jet using the k–ε and second moment closure turbulence models

M. Nishimura[1,*,†] and N. Kimura[2]

[1] *Power Plant Engineering Division, Kawasaki Heavy Industries, Ltd., 2-6-5, Minamisuna, Koto-ku, 136-8588 Tokyo, Japan*
[2] *New Technology Development Group, O-arai Engineering Center, Japan Nuclear Cycle Development Institute, Narita, O-arai, Ibaraki 311-1393, Japan*

SUMMARY

Low Reynolds number turbulence stress and heat flux equation models (LRSFM) have been developed to enhance predictive capabilities. A new method is proposed for providing the wall boundary condition for dissipation rate of turbulent kinetic energy, ε, to improve the model capability upon application of coarse meshes for practical use. The proposed method shows good agreement with accepted correlations and experimental data for flows with various Reynolds and Prandtl numbers including transitional regimes. Also, a mesh width about 5 times or larger than that used in existing models is applicable by using the present boundary condition. The present method thus enhanced computational efficiency in applying the complex turbulence model, LRSFM, to predictions of complicated flows. Unsteady Reynolds averaged Navier–Stokes (URANS) computations are conducted for an oscillatory non-isothermal quasi-planar triple-jet. Comparisons are made between an experiment and predictions with the LRSFM and the standard k–ε model. A water test facility with three vertical jets, the cold in between two hot jets, simulates temperature fluctuations anticipated at the outlet of a liquid metal fast reactor core. The LRSFM shows good agreement with the experiment, with respect to mean profiles and the oscillatory motion of the flow, while the k–ε model under-predicts the mixing due to the oscillation, such that a transverse mean temperature difference remains far downstream. Copyright © 2003 John Wiley & Sons, Ltd.

KEY WORDS: transitional flow; thermal striping; mixing of jets; Reynolds stress equation; turbulent heat flux equation; liquid metal cooled fast reactor

1. INTRODUCTION

Predictions with a turbulence model based on the Reynolds averaged Navier–Stokes equation (RANS) have been one of the most popular ways for design assessment in the industrial field. Generally, engineers aim to extract information on thermal-hydraulic performance under rated, partial or transient conditions, via predictions assuming steady or quasi-steady states.

*Correspondence to: M. Nishimura, Power Plant Engineering Division, Kawasaki Heavy Industries, Ltd., 2-6-5, Minamisuna, Koto-ku, 136-8588 Tokyo, Japan.
†E-mail: nishimura_mo@khi.co.jp

Received 3 March 2002
Revised 22 November 2002

However, applying high-performance computing with a fine computational grid and a higher-order convective differencing scheme often exhibits oscillatory motions of the flow fields. The oscillations arise from the flow instabilities that are often encountered in complex industrial systems.

Tucker and Pan [1] performed unsteady RANS (URANS) computations for a complex flow in the model of an electronic device. They made comparisons of mean and unsteady component of velocity distributions between the experiment and predictions with a wide spectrum of zero to two-equation turbulence models, showing similarity of mean velocity and significant variation of velocity fluctuation intensity among the predictions. Unsteady heat transfer characteristics were investigated on separated flows in a duct with rib turbulators by Tatsumi *et al.* [2] applying URANS with a non-linear eddy viscosity model. They suggested serious influence of a large time scale periodic fluctuation on instantaneous thermal-hydraulic fields. Maekawa [3] carried out transient computations on thermal stratification in the upper plenum of a test rig simulating a liquid metal cooled fast reactor in which the rising speed and temperature gradient of the stratified boundary were the important parameters to be predicted. The transient was quasi-steady states with respect to the system parameters such as flow rate, inlet temperature, etc. The computation though, showed an oscillation of the jet discharged from 7 circular nozzles, simulating the reactor core outlet, into the hot plenum and a sloshing motion of the stratified boundary. Also the oscillatory jet impinged upon the thermal stratification boundary, shaving and entraining the hot fluid particles above the boundary.

The above work shows the URANSs capability of predicting unsteady flows featuring the eddy viscosity models. The complex flows, however, may have anisotropy of eddy viscosity as well as different time scales in directions, $\overline{u_i u_i}/\varepsilon$. The present work examined the applicability of low Reynolds number turbulence stress and heat flux equation models (LRSFM) and the standard k–ε model, focusing on the coherent oscillatory motion as well as time averaged characteristics. Also, a low Reynolds number wall boundary condition approach ε is proposed to improve the model when a coarse mesh is utilized for practical application. Some results from validation studies are presented to show accuracy and computational efficiency of the proposed boundary condition and the LRSFM.

A comparative study of the turbulence models was carried out through calculations for a water test of three quasi-planar jets conducted by Kimura and Tokuhiro *et al.* [4, 5]. Thermal striping phenomena was simulated; the convective mixing and temperature fluctuations anticipated at the outlet of a liquid metal cooled fast reactor core. This phenomenon may affect the integrity of structures exposed to such fluctuations. The water experiment involves the thermal mixing of an unheated central jet (referred to as 'cold') in between two adjacent jets at a higher temperature (referred to as 'hot') and at the same discharge velocity relative to the central jet. In this paper, a comparison along with a discussion of the experiment and the numerical simulations are presented. The typical characteristics of mixing of thermal jets under specified conditions are discussed.

2. EXPERIMENT

Figure 1 shows the experimental apparatus. The test section is immersed inside a rectangular tank measuring in mm $2438 \times 2438 \times 671$. As noted in the top view, two acrylic partition plates sandwich four rectangular blocks, thereby confining the jets into a quasi,

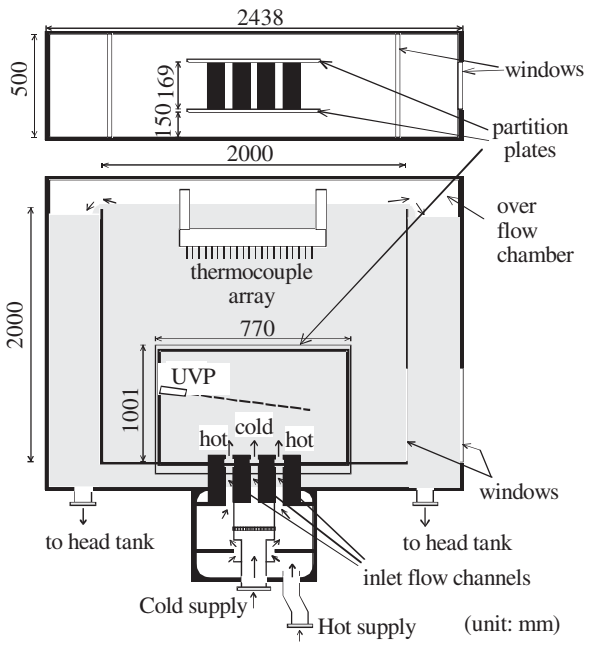

Figure 1. Schematic illustration of the experimental apparatus.

two-dimensional planar flow. The size of the nozzles is $20 \times 169\,\text{mm}^2$. Additional details on the facility are contained in the studies by Kimura *et al.* [4] and Tokuhiro *et al.* [5]. Temperature measurements were taken with a traversing thermocouple array consisting of 39 K-type, chromel-alumel thermocouples (TCs) facing vertically downward and horizontally spaced in 5 mm intervals over a 190 mm span. The expected measurement error is less than 0.1°C. The TCs are inserted and bonded to the horizontal bridge and are threaded into either the right or left arms.

Velocity measurements were taken using the Met-Flow Model X-1 Ultrasound Velocity Profile (UVP) [6, 7] monitor with a single, Delrin-encased (temperature limit ~ 80°C) piezoelectric transducer with a 6 mm diameter beam, operating at 4 MHz.

3. PREDICTIVE TECHNIQUE

3.1. Conservation equations

A complete description of the conservation equations and turbulence model is presented in the appendix. Here, we only present a summary and note features of the turbulence model. The ensemble averaged equations of mass, momentum and energy (specific enthalpy) are implemented in the single phase multi-dimensional code CASCADE [8, 9]. In this set of equations, second-order moments such as Reynolds stress, $\overline{u_i' u_j'}$, and turbulent heat flux, $\overline{u_i' h'}$ appear. The most popular way to calculate these moments is to use k–ε models in which isotropic eddy viscosity and a linear relation between the second-order moments and its associated mean field

gradient are assumed. In the present study, the conservation equations of Reynolds stress and the turbulent heat fluxes are solved to eliminate unwanted contributions originating from the assumptions used in the k–ε models as just mentioned. In the case of sodium flow, the turbulent Prandtl number is dependent on the Reynolds number as well as on space. This is because of the small 'laminar' Prandtl number of liquid sodium. Therefore, we abandon the use of the turbulent Prandtl number and solve for the turbulent heat fluxes as dependent variables.

The Reynolds stress equation model (RSM) implemented here was proposed by Shima and validated for various types of flow such as a flat plate boundary layer [10], a boundary layer with transpiration [11], a rotating channel flow [12], and a three-dimensional turbulent boundary layer on a swept wing [13], etc. The turbulent heat flux equation model (HFM) used in this study is based on a model proposed by Launder [14]. In the present model, the fluctuating pressure-specific enthalpy correlation is modified:

$$\Phi_{it} = \Phi_{it1} + \Phi_{it2} + \Phi_{it3} + \Phi_{itw} \tag{1}$$

where

$$\Phi_{it1} = -C_{t1}\frac{\rho\varepsilon}{k}\overline{u_i'h'} - C_{t1n}\frac{\rho\varepsilon}{k}a_{ij}\overline{u_j'h'} \tag{2}$$

$$\Phi_{it2} = -C_{t2}(P_{it1} + P_{it2}) \tag{3}$$

$$\Phi_{it3} = -C_{t3}G_{it} \tag{4}$$

$$\Phi_{itw} = C_{t1}'\Phi_{kt1}n_k n_i \frac{k^{3/2}}{C_l \varepsilon x_n} \tag{5}$$

$$P_{it1} = -\rho\overline{u_i'u_k'}\frac{\partial\bar{h}}{\partial x_k} \tag{6}$$

$$P_{it2} = -\rho\overline{u_k'h'}\frac{\partial U_i}{\partial x_k} \tag{7}$$

with n as a unit vector normal to the wall and its use as a subscript stands for the normal direction. The quantity a_{ij} is the dimensionless, anisotropic representation of Reynolds stress:

$$a_{ij} = \frac{\overline{u_i u_j}}{k} - \frac{2}{3}\delta_{ij} \tag{8}$$

A description of other notations is contained in the appendix. There are two differences in the above equation compared to Launder's model. The last term in Equation (2) was added to simulate the anisotropy of turbulence. Also, in a conventional HFM, P_{it1} is ignored in Equation (3). The importance of the presence of this term in Equation (3) was, however, shown by Nishimura *et al.* [15] in the computation of gas flows at high heat fluxes accompanied by laminarization.

3.2. Wall boundary conditions

A non-slip wall boundary condition was applied to the top and the side faces of the nozzle blocks. The side faces of the nozzle blocks corresponded to channel walls of the inlet nozzles (see Figure 1).

The Reynolds stress equation model proposed by Shima [10] used a boundary condition for ε_w which is similar to other low Reynolds number models. Its form is as follows:

$$\varepsilon_w = \nu \frac{\partial^2 k}{\partial y^2} \tag{9}$$

or

$$\varepsilon_w = 2\nu \left(\frac{\partial \sqrt{k}}{\partial y} \right)^2 \tag{10}$$

Equations (9) and (10) are identical to each other in a mathematical sense, except that, Equation (10) has the advantage of stability in terms of numerical calculations [16]. However, to maintain accuracy during calculations, one has to place the computational node of the wall-bounded control volume very close to the wall such that the non-dimensional distance y^+ is less than 0.5 (e.g. Reference [16]). For example, this non-dimensional distance corresponds to several μm for sodium flow with a Reynolds number on the order of 10^5, a pipe diameter of 0.05 m, an average temperature of 300°C, and an average velocity of 1 m/s. So this criterion makes the actual application of low Reynolds number models difficult, not only for large-scale power plants, but also for sodium flows at experimental facilities. Therefore, we sought to implement a new method such that one could use a coarse mesh arrangement near walls. This new type of wall boundary condition was applied to ε, and it enhanced the efficiency and robustness of computations. From dimensional analysis, ε can be expressed as follows:

$$\varepsilon \propto \frac{k^{3/2}}{l} \tag{11}$$

where l is a characteristic length of eddies. The most common expression based on this relation is used in the wall function from a log law (e.g. Reference [17]) as

$$\varepsilon = \frac{C_\mu^{3/4} k^{3/2}}{\kappa y} \tag{12}$$

where C_μ and κ are empirical and von Karman constants, respectively. This equation was applied to the first node from the wall to provide a boundary condition for ε in high Reynolds number turbulence models. We note that in this case, the first node should be placed in the region between $30 < y^+ < 200$, where the logarithmic velocity profile is formed. In practice, many codes with high Reynolds number models use this equation from $y^+ = 12$. The lower limit of validity of Equation (12) is due to changes of C_μ and κ in the near wall region, $y^+ < 12$, where the velocity profile deviates from the log law due to influence by fluid viscosity. In the present work, we propose to modify and extend the relation, Equation (11), to the near wall region by replacing the constant part of Equation (12) with a function of y^+ as follows:

$$\varepsilon = f_{\text{eps}}(y^+) \frac{k^{3/2}}{y} \tag{13}$$

where

$$f_{\text{eps}}(y^+) = \max[0.19, 7.90\,(y^+)^{-1.89}] \tag{14}$$

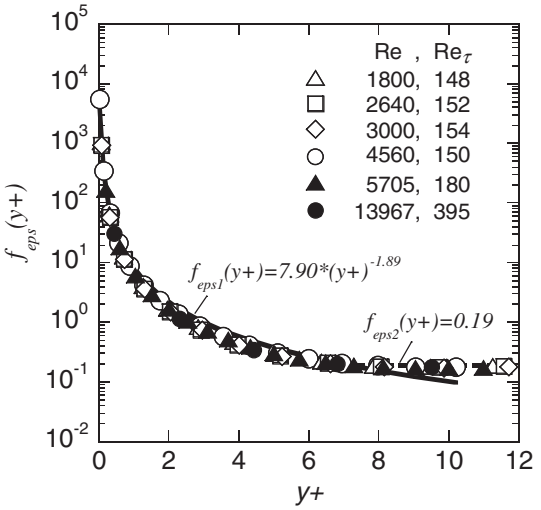

open symbols: Kuroda et al. (1997),
close symbols: Kawamura (2000)

Figure 2. Function providing ε wall boundary condition.

Equation (13) is also applied to the first node from the wall, as in Equation (12), but not at the wall itself. The above function is shown in Figure 2 and derived from regression applied to the data taken from the DNS database of Kuroda *et al.* [18] and Kawamura [19]. The former calculation was executed for turbulent plane channel flow and the latter for turbulent circular tube flow. We note that Equation (14) takes directly into account neither the Reynolds number nor the type of flow. Nevertheless, the effect of Reynolds number is implicitly contained in Equation (14) via y^+ and k and thus u_τ.

To check the applicability of Equation (13) to flows under various Reynolds number conditions, Nishimura [20] conducted validation studies for fully developed pipe flow of a fluid with Prandtl number, $Pr = 1.0$, including its turbulent–laminar transition and separately the heat transfer coefficient of the liquid sodium ($Pr \approx 0.0044$ at 580°C) flow in a circular tube. The predictions using Equation (13) were performed using meshes with the first node placed at distances $y^+ < 0.5$ (fine mesh) and $y^+ < 5$ (coarse mesh) from the wall. Figure 3 presents comparisons of the predicted results to the accepted correlations for the flow at $Pr = 1.0$. In the figure, the notations 'FM' and 'CM' denote fine and coarse meshes, respectively. Also, 'Axi-CM' is the results obtained using an axial mesh with twice the length of that in CM. The distance of the first node applied to the coarse mesh is 5 times or larger compared to that being used in conventional low Reynolds number turbulence models. The label 'mod Dittus-Boelter' stands for the popular relation with the modified coefficient [21]:

$$Nu = 0.021\, Re^{0.8} Pr^{0.4} \tag{15}$$

The predicted results show a near stepwise transition at $Re = 2.4 \times 10^3$–2.5×10^3 and 2.3×10^3–2.4×10^3 for the fine and coarse meshes, respectively, and good agreements to the correlations. In addition, a representative CPU time using the fine and coarse meshes were 88 and 5 min,

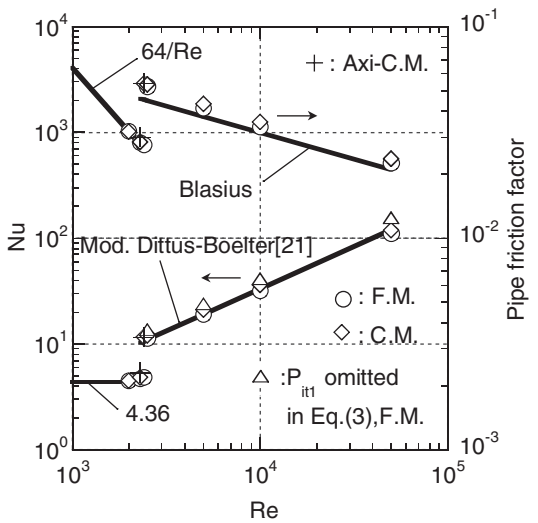

Figure 3. Influence of modelling of the flux equations and mesh width on predicted Nusselt number and friction factor.

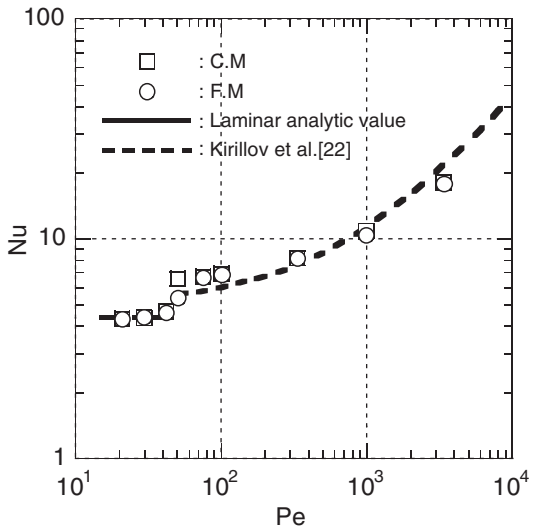

Figure 4. Comparisons of predicted and correlated sodium flow heat transfer dependence on Peclet number.

respectively, for a calculation at $Re = 1 \times 10^4$ on FACOM VPP-300 which had a maximum potential of 1 GFLOPS. These results show that the present model is capable of predicting transitional flow with both fine and coarse meshes with improved computational efficiency. In Figure 4, the calculated results from the present model with the boundary condition (13) are compared to empirical and analytic values for liquid metal flow in turbulent and laminar

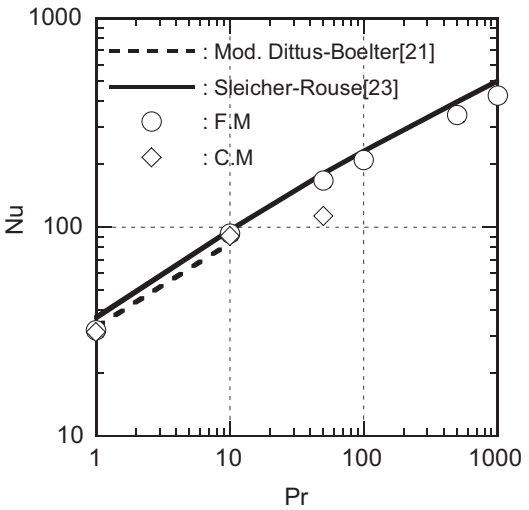

Figure 5. Comparisons of Nusselt numbers among prediction and correlations for fluids at higher Prandtl numbers.

flow regimes, respectively. The first node from the wall was placed closer than $y^+ = 0.5$ for the fine mesh arrangement, while for the coarse mesh, the first node was at about $y^+ = 4$. The analytic value of the Nusselt number for laminar flow is 4.36. For the turbulent regime, the empirical correlation by Kirillov *et al.* [22]:

$$Nu = 5 + 0.025Pe^{0.8} \tag{16}$$

was selected for comparison. The prediction traces heat transfer dependency on Peclet number well. Moreover, the results from the fine and coarse mesh calculations show the same Nusselt numbers except in the transitional Peclet number region.

Predictive capability of the present model was also examined on Nusselt numbers for the fluids with higher Prandtl numbers at $Re = 1 \times 10^4$. The correlations of modified Dittus–Boelter and Sleicher–Rouse [23] are cited to make comparisons with the prediction. Sleicher and Rouse presented correlation to determine Nusselt numbers for various values of Reynolds and Prandtl numbers:

$$Nu = 5 + 0.015\, Re^a Pr^b \tag{17}$$

where

$$a = 0.88 - 0.24/(4 + Pr) \tag{17a}$$

$$b = 1/3 + 0.5\mathrm{e}^{-0.6Pr} \tag{17b}$$

As shown in Figure 5, predicted heat transfer coefficients at the cross-section $200D$ from the inlet, under the fully developed condition, are compared to the accepted correlations [21, 23]. The computed result with the fine mesh agrees well with the correlations, showing that the

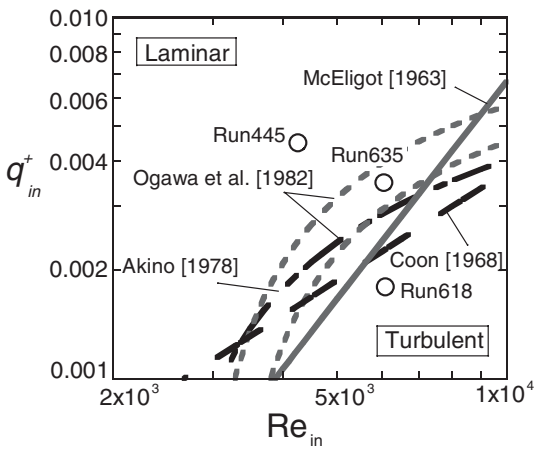

Figure 6. Criteria for flow regime prediction and the experimental conditions of Shehata [25].

present model is capable of predicting heat transfer for high Prandtl number fluid flow. On the other hand, the result with the coarse mesh fails to predict the Nusselt number at $Pr = 50$. This can be attributed to the location of the first computational node from the wall, placed at $y^+ \approx 2.5$. The thickness of a thin conduction wall sublayer is 1/50th than that of a viscose wall sublayer in the fluid flow at $Pr = 50$. Thereby, the coarse mesh is not able to resolve the steep temperature gradient in the vicinity of the wall.

As for the last validation study on the present model and the wall boundary condition, predicted results are presented on the forced convection gas flows in a circular tube at high heat fluxes accompanied by laminarization [15]. The high heat flux on the wall, e.g. applied in gas-cooled reactors, imposes significant gas temperature variation along and/or across the cooling channels on turbulent flow. The temperature range causes variation of the gas properties, invalidating the use of design relations such as the popular Dittus-Boelter correlation [24]. Therefore, the laminarization is one of the important thermal-hydraulic issues to be well predicted with computational codes. In the present study, the experiment conducted by Shehata [25] was computed. A resistively heated, seamless, extruded Inconel 600 tube of 27.4 mm (1.08 in) inside diameter was employed as the test section. Heated length between the electrodes was about 32 diameters and it was preceded by a 50 diameter, adiabatic entry region for flow development. Criteria for flow regime prediction [26] and experimental conditions are presented in Figure 6. Runs 618, 635 and 445 are corresponding to inlet Reynolds numbers of about 6080, 6050 and 4260 with non-dimensional heating rates, $q^+ = q''_w/(G\, c_p\, \Theta_i)$, of about 0.0018, 0.0035 and 0.0045, respectively. Figure 7 shows comparisons of Nusselt numbers between the experiment and the prediction. The origin of x-axis is set at the start point of heated wall. Agreement of the predictions with the experiment is good. The maximum error occurs in case 635 for the result of CM at $x/D = 22.5$. The computation over-predicted the Nusselt number as about 13% compared to the experimental data. The differences between the predictions and the data, however, are still comparable to the estimated experimental uncertainties in general. Mean velocity and temperature profiles at $x/D = 24.54$, near the top end of the resistively heated section, are presented in Figures 8 and 9, respectively. The

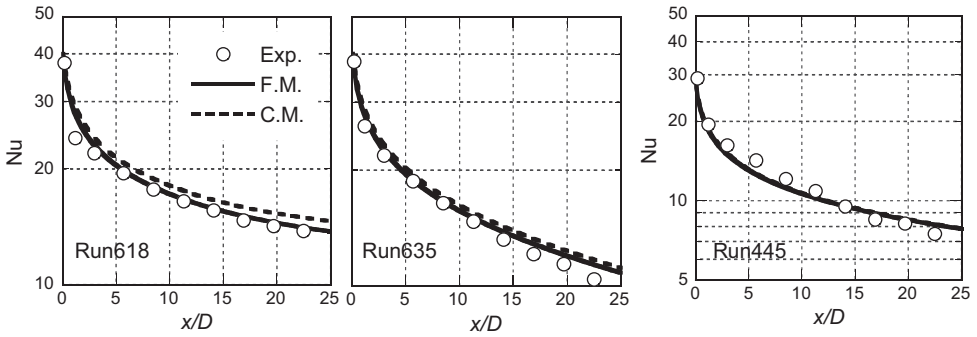

Figure 7. Comparisons of wall heat transfer parameters.

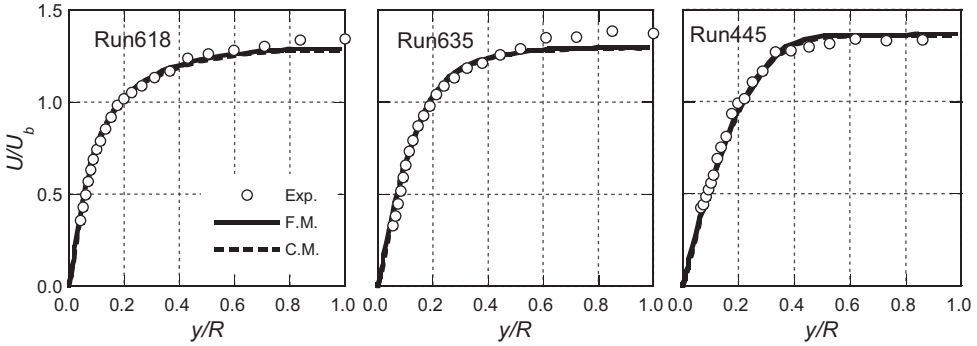

Figure 8. Comparisons of mean velocity profiles at $x/D = 24.54$.

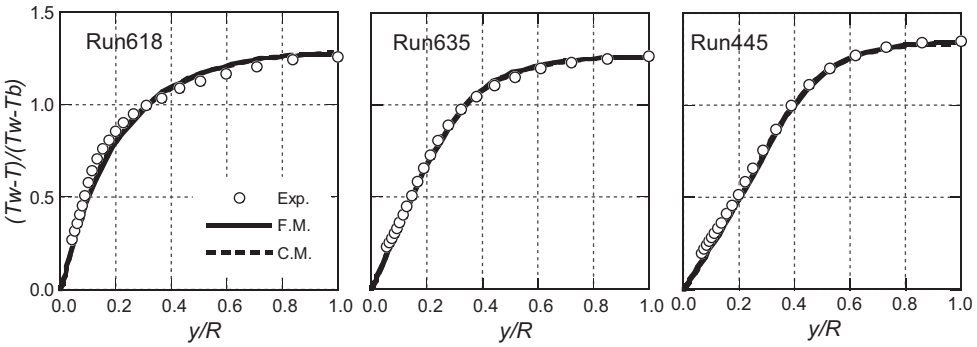

Figure 9. Comparisons of mean temperature profiles at $x/D = 24.54$.

computation consistently agrees to the experiment. This shows that the present model is capable of predicting laminarization due to strong heating as well as that caused by the change of Reynolds number, even if coarse meshes are applied.

We note that a Taylor-series expansion of the equations for turbulence quantities at the wall yields that the order of magnitude of ε is mainly determined by y^0; i.e. ε approaches to a certain value with decreasing y while k is proportional to y^2 (e.g. Reference [27]). If one apply this relation of k with y to Equation (13), the new boundary condition (13) for ε is proportional to $y^{0.11}$; the numerator and denominator are, respectively, proportional to y^3 and $y^{2.89}$, which nearly agrees with the result of a Taylor-series expansion of ε. We could match the near wall behaviour of ε, as $\varepsilon \propto y^0$, by setting the power of y^+ to -2.00 instead of -1.89 in Equation (14). Strictly speaking, however, the Taylor series expansion of ε can be written as follows [27]:

$$\varepsilon = \nu\{(a_1'^2 + c_1'^2)y^0 + 4(a_1'a_2' + c_1'c_2')y^1\} + \cdots \tag{18}$$

Thus ε contains contributions from $\propto y^1$ as well as $\propto y^0$. Meanwhile, our functional ε wall boundary condition is derived from a DNS database, shown by the regression in Figure 2. The DNS results for some range of Reynolds numbers correlated very well with Equation (14). One expects that the linear contribution to term ε is associated with the term $\varepsilon \propto y^{0.11}$. This trend is inherently reflected in the DNS result. The value of the exponent, 0.11, makes ε nearly constant around the region of $y^+ = 0.1$ to 1, where the first node is placed in the use of Equation (13). This implies consistency of the present boundary condition with the asymptotic behaviour of ε in the near wall region.

As for other turbulence quantities than ε, featured in the LRSFM, namely $\overline{u_i'u_j'}$, $\overline{u_i'h'}$ and $\overline{h'h'}$, values are equal to zero at the wall. With the k–ε model prediction, the log law wall function was used to set the wall boundary conditions.

3.3. Inlet conditions

For the simulation of the jets, distributions of the dependent variables are specified as an inlet boundary condition, at the horizontal cross-sections approximately 60 mm upstream from the nozzle outlets. These distributions are predicted previously and separately from the computation of the jet and determined via calculation of channel flow in the entrance region, which has a 20 mm width and 340 mm length, that existed upstream of the computational region for the jets. At the inlet of the entrance region, uniform distributions of the dependent variables are assumed, and the following values are applied:

$$W_{\text{in}} = 0.5\ \text{m/s}, \quad T_{\text{h}} = 30.8^\circ\text{C}, \quad T_{\text{c}} = 25.4^\circ\text{C}, \quad k = 0.005W_{\text{in}}^2, \quad \varepsilon = \frac{C_\mu^{0.75}k^{1.5}}{0.09 \cdot D}, \quad C_\mu = 0.09$$

$$\overline{u'u'} = \overline{v'v'} = \overline{w'w'} = \tfrac{2}{3}k, \quad \overline{u'w'} = 0, \quad \overline{h'h'} = 0, \quad \text{and} \quad \overline{u'h'} = \overline{w'h'} = 0$$

Both T_{h} and T_{c} correspond to the measured values.

The average discharge velocity and temperature difference between the jets gives a typical Richardson number, $Ri_{\text{exp}} \approx 0.002$, for $Gr_{\text{exp}} \approx 4.5 \times 10^5$ and $Re_{\text{exp}} \approx 1.5 \times 10^4$. In a LMFR at the rated conditions, the corresponding Ri number, for $Re_{\text{LMFR}} \approx 1.7 \times 10^6$ and $Gr_{\text{LMFR}} \approx 3.1 \times 10^9$, is typically around $Ri_{\text{LMFR}} \approx 0.0014$. Thus, the flow in both the experiment and a typical LMFR is dominated by forced convection.

3.4. Outlet conditions

For the momentum equations, velocity components normal to the outlet boundary surfaces are specified to satisfy the mass conservation law of the outlet control volumes. For the energy and the turbulence equations, a zero gradient normal to the boundary is applied. A constant value of the pressure is specified at the outlet control volumes, as a Dirichlet pressure boundary condition.

3.5. Computational grid

A two-dimensional Cartesian co-ordinate system is used for the calculations since the thermal-hydraulic field under consideration is assumed to be planar. The typical mesh size is 2.0–3.0 mm for the region where the main flow passes. The variable mesh used with the LRSFM consists of 160×170 control volumes spanning a 460 mm $\times$ 668 mm (width $\times$ height) simulation domain, including the upstream part of the nozzle channel with a length of 59 mm. For the prediction with the k–ε model, a variable mesh 150×193 is applied over a 763 mm $\times$ 932 mm computational region (also includes part of the nozzle channel). Thus the extents of the computational regions are different for the calculations of the LRSFM and the k–ε model. We therefore checked the possible influence caused by this difference by means of calculations with the k–ε model. We found no substantial influence caused by the difference of computational regions used in the present calculation. The highest aspect ratio of the computational mesh is 25 on the line in contact with the top face of the nozzle blocks, near the side edge of the computational region. The high aspect ratio meshes also exist on the line in contact with the nozzle channel walls, near the top of the computational region. If we use the existing wall boundary condition (10) instead of the proposed Equation (13), we have to set a thinner mesh on the walls of the nozzle blocks, which will lead to an aspect ratio higher than 100 and subsequently make us use a finer mesh arrangement. In the case of applying existing condition (10) to coarse meshes, the solution may often be wrong [20]. This may affect the behaviour of the jet via erroneous distributions of velocity and turbulence quantities at the nozzle outlet. Consequently, the present wall boundary condition for ε is useful to keep high computational accuracy and efficiency.

3.6. Numerical method

The numerical algorithm employed in the CASCADE code is SIMPLEST-ANL [28]. Skew upwind and central differential schemes are applied to the convection and diffusion terms, respectively, for the conservation equations.

Unsteady calculations are performed with a time step of 0.001 s and a maximum outer iteration number of 20. For the convergence test of the unsteady calculation, we changed the time step interval from 0.0005 to 0.002 and the maximum outer iteration number from 10 to 50. Within such a range of computational condition, no substantial difference was found among the solutions. The maximum variation of velocity components between the last two outer iterations in each time step is in the order of 10^{-6} m/s. In addition, the maximum relative variation of specific enthalpy between the last two outer iterations in each time step is in the order of 10^{-8}.

4. RESULT AND DISCUSSION

Plate 1 shows a comparison of the experimental, visualized flow field and the results of simulations. The flow visualization experiment was conducted by injecting Rhodamine dye into the side jets in contrast to the central jet while illuminating with an argon laser sheet. As for the simulations, colour contours of the temperature fields are as shown. These pictures depict a representative 1/15th-of-a-second time sequence of the oscillating triple-jet. In the region just downstream of the nozzles, the central jet appears straight and two side jets lean and bend toward the central jet. Afterward the three jets converge into a single stream. Both predictions reproduced the convergence of the jets. However, the k–ε model under-predicts the transverse swaying motions of the jets, especially for the central jet. Meanwhile the LRSFM case shows a coherent oscillatory motion of the jets as seen in the experiment; the central jet sways and meanders, the boundary of the intermittent region of the outer jets is wavy. In both the experimental and the LRSFM results, note the initial location where the central jet sways to the right, as the left jet redirects itself toward the right, and vice versa. This gives the impression that the exterior jets alternately 'push' the central jet. In the composite jet region, the branches of hot fluid within the central cold region of the triple-jet, tends to homogenize the time-averaged distribution of temperature. On the other hand, the k–ε model predicts no active oscillatory motion in the composite jet region. The results thus presented indicate the significance of the coherent oscillatory motions to the mixing of non-isothermal jets. The LRSFM is capable of reproducing this oscillation.

A comparison of the fluctuating temperature trends versus time between the experiment and the LRSFM prediction is presented in Figure 10. The time series of fluctuations are nearly sinusoidal for both results, revealing the influence of the coherent oscillatory motion of the jets. On the other hand, the experiment contains random components in addition to the sinusoidal trend. The peak-to-peak temperature difference is about 5°C for both results. However, the typical temperature difference in one cycle of the experiment is apparently less than 5°C, while the LRSFM consistently predicted a 5°C difference. This difference is highlighted by the root-mean-square value of temperature, which will be presented later.

A comparison of the auto-power spectral density of temperature is shown in Figure 11. As shown, the LRSFM correctly simulates the prominent frequency of 2.25 Hz, the periodicity attributed to the sinusoidal fluctuation presented in Figure 10. The LRSFM also shows two harmonics of the prominent frequency, while harmonics and sub-harmonics of smaller amplitude are seen in the experiment. The k–ε model, on the other hand, under-predicts the prominent frequency as being 1.5 Hz. The lower prominent frequency and dampened swaying

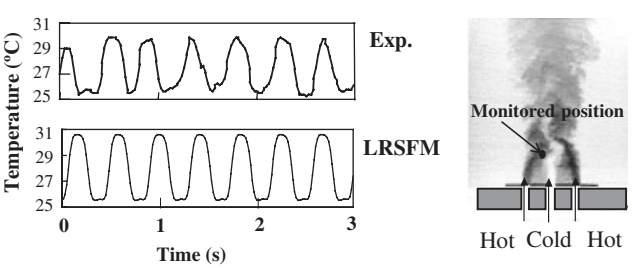

Figure 10. Time trends of temperature fluctuations.

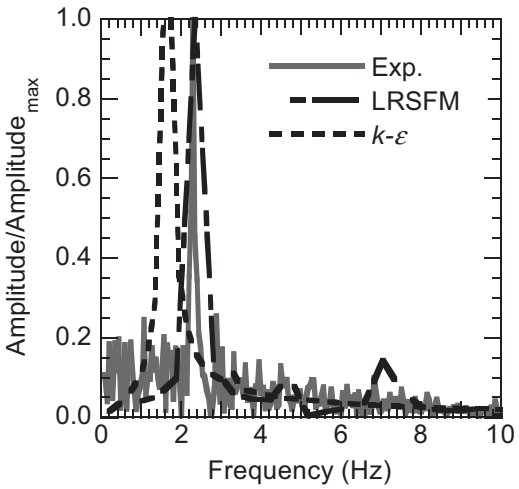

Figure 11. Comparison of auto-power spectral density of temperature fluctuation.

motion predicted by the k–ε model are mainly attributed to over-prediction of the eddy viscosity in the mixing region. Numerical diffusion is possibly another reason for damping of the oscillation. However in the present case, numerical diffusion is not a source of the damping because the same convective differential (skew upwind) and time integration schemes (implicit Eulerian), as well as the same time step intervals of 0.001 s and similar mesh sizes, were used in both predictions. The reason for the low turbulence level and hence the eddy viscosity of the LRSFM result is due to a coefficient in the production term of the ε equation. A function is implemented for the coefficient instead of using an empirical constant that is popular way for the k–ε model and high Reynolds number type RSMs. The function takes account of turbulence anisotropy. In the jet flow region, i.e. not in the nozzle, the function gives a higher value than the fixed empirical constant leading larger productions of ε. This subsequently leads to higher values of ε in the LRSFM calculation compared to the k–ε model. The relatively high value of ε keeps the turbulence level low in the LRSFM calculation. Note that at the exit plane of the nozzles, the flow is fully developed. Also the intensities of turbulence are the same magnitude between the LRSFM and the k–ε model. Therefore, the difference of the results between the LRSFM and k–ε model does not originate from the turbulence characteristics in the nozzle channels; that is the wall boundary conditions, the log law or the low Reynolds number treatment, have no influential on the solution in the present case. Also as we did not present in any figures in the present paper, a calculation with the high Reynolds number RSM was also performed using the standard ε equation. This simulation showed an intermediate result between the LRSFM and the k–ε model, with respect to the amplitude and frequency of the oscillatory motion.

Comparisons of mean temperature profiles in transverse directions are shown in Figure 12. In the figure, $D = 35.8$ mm; is the hydraulic diameter of the rectangular nozzle. At the downstream location, $z/D = 0.55$ ($z/D = 0$ at nozzle exit), the LRSFM agrees well with the experiment while the sharp gradients on either side of the cold jet are under-predicted by the k–ε model. Both models show the same profile and under-prediction of mixing at the cold

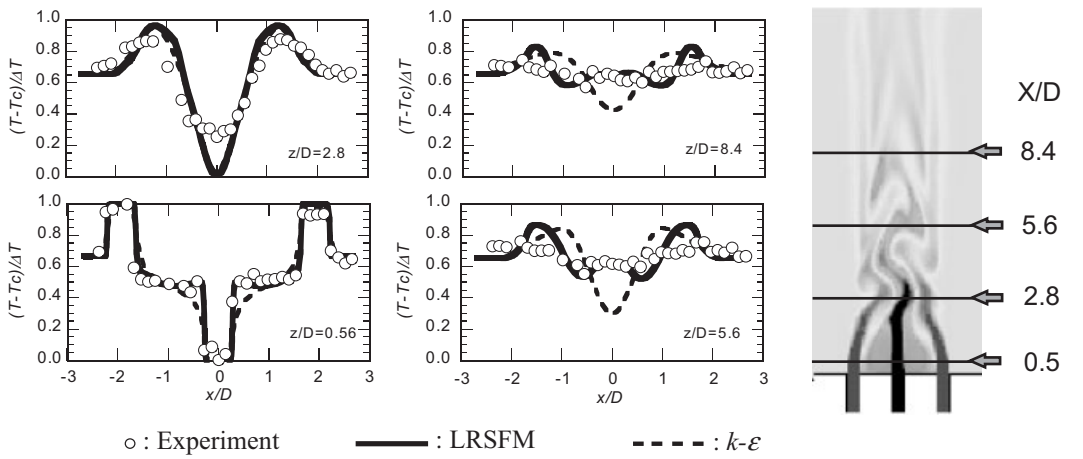

Figure 12. Comparison of horizontal temperature profiles.

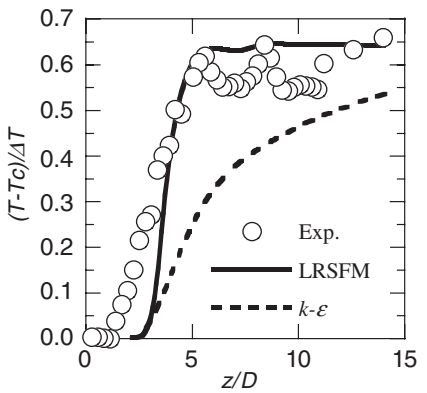

Figure 13. Axial distributions of mean temperature at the centreline.

jet, at $z/D = 2.8$. At $z/D = 5.6$ and 8.4, the apparent differences are shown in both the central and outer regions; the LRSFM shows a smaller discrepancy with respect to the experiment than the k–ε model. The latter clearly shows the unmixed region of cold fluid. Both models over-predict the temperature along the outer regions of the stream at $x/D = \pm(1.0\text{–}1.5)$.

The axial distribution of mean temperature at the centreline ($x/D = 0$) is plotted in Figure 13. Overall, the LRSFM follows the axial temperature increase seen in the experiment. The increase is, however, delayed and abrupt. On the other hand, the k–ε model predicts a gradual temperature increase which is markedly different from the experiment. The rapid temperature increase corresponds to the location of the coherent oscillation of the jets in the experiment and LRSFM result. Thus, the oscillation significantly contributes to the mixing of the jets.

Next, the temperature fluctuation is discussed, featuring the contribution of the coherent oscillation. To treat temperature fluctuations arising from the coherent oscillation and

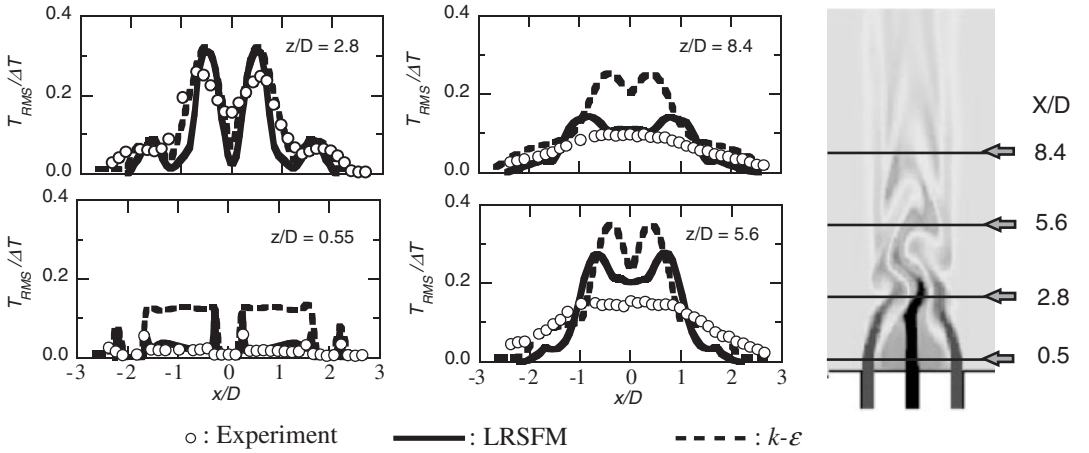

Figure 14. Comparisons of temperature fluctuation intensity profiles.

turbulent flow, we introduce the following decomposition of instantaneous temperature t by the expression:

$$t = T + \tilde{t} + t' \tag{19}$$

where T is the mean temperature, $\tilde{t}$ is the periodic component due to contribution of the coherent oscillation and t' represents random or incoherent turbulent motion [29, 30]. Then the root-mean-square value, the intensity of temperature fluctuation, T_{RMS}, is written as

$$T_{\mathrm{RMS}} = \sqrt{\overline{\tilde{t}^2} + \overline{t'^2} + 2\overline{\tilde{t}t'}} \tag{20}$$

We can readily calculate T_{RMS} from the experimental data in which the instantaneous temperature t is acquired. On the other hand in a numerical simulation, the Reynolds averaged conservation equations with a turbulence model provide temperature fluctuations due to the coherent oscillation and turbulence of the jets separately. Namely, we performed the unsteady calculation with a time step interval of 0.001 s. Therefore, the simulation reproduces a composite jet oscillation accompanied by a sinusoidal temperature fluctuation $(T + \tilde{t})$ (see Figure 10), in addition to the turbulent fluctuation of temperature $\overline{t'}$ calculated from the $\overline{h'h'}$ equation. Thus Equation (20) should be used to calculate T_{RMS}. We note, however, that according to Reynolds *et al.* [29], the cross term of coherent and turbulence fluctuations is, by definition, $\overline{\tilde{t}t'} \approx 0$, since the time-scales of the fluctuations are completely different. Hence no correlation is expected between them. In fact, a data analysis of our experiment shows that $\overline{\tilde{t}t'}$ is less than 5% of T_{RMS} when calculated by Equation (20) within the region where the coherent oscillation shows the maximum amplitude.

Comparisons of intensity of temperature fluctuations between the experiment and the predictions are shown in Figure 14. Again, relative agreement between the LRSFM and the experiment is better than with the k–ε model. The k–ε model consistently over-predicts the fluctuation in the region in between the jets. At $z/D = 0.55$, the experiment and the LRSFM show small intensity of temperature fluctuations in between the jets $(0.3 < |x/D| < 1.7)$.

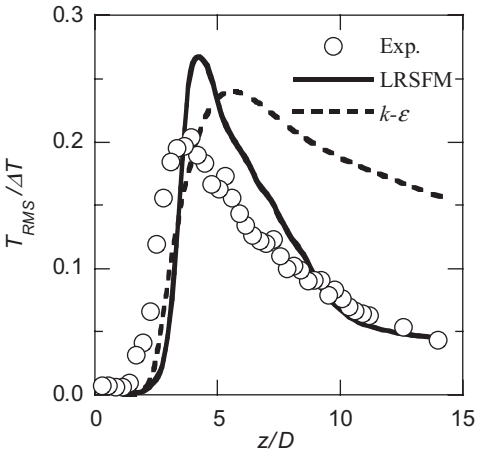

Figure 15. Axial distributions of temperature fluctuation intensity at the centreline.

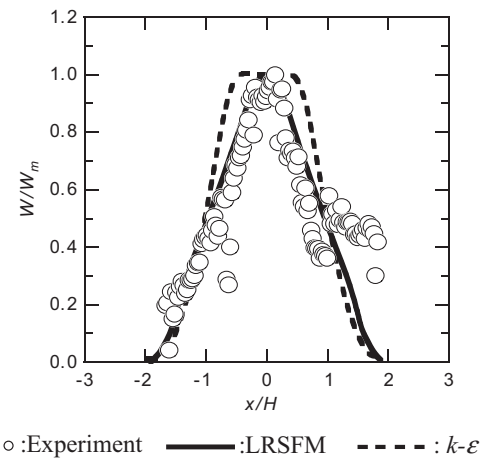

Figure 16. Comparisons of mean velocity profiles at $z/D = 8.4$.

However, the k–ε model significantly over-predicts the intensity. Figure 15 presents axial distributions of temperature fluctuation intensities at the centreline. Here too, the LRSFM captures the trends in both development and decay of the temperature fluctuation in comparison to the experiment while the peak value is excessively high. In contrast the k–ε model correctly predicts the initial increase in T_{RMS} but poorly simulates the decay of the fluctuation; that is, the disagreement is similar to the axial distribution of mean temperature seen in Figure 13. This poorly simulated mixing based on the k–ε model is consistent with the persistence of the transverse temperature gradient in Figure 12 at $z/D = 5.6$ and 8.4. Here again, for $z/D > 5$, T_{RMS} calculated with the k–ε model is greater than that in the experiment; the lack of mixing due to coherent oscillation is apparent in the mean temperature profile.

Next, we show the mean velocity profiles at $z/D = 8.4$ in Figure 16. In this figure, we apply popular non-dimensionalization in which the centre-line velocity, W_{m}, and half-width of the

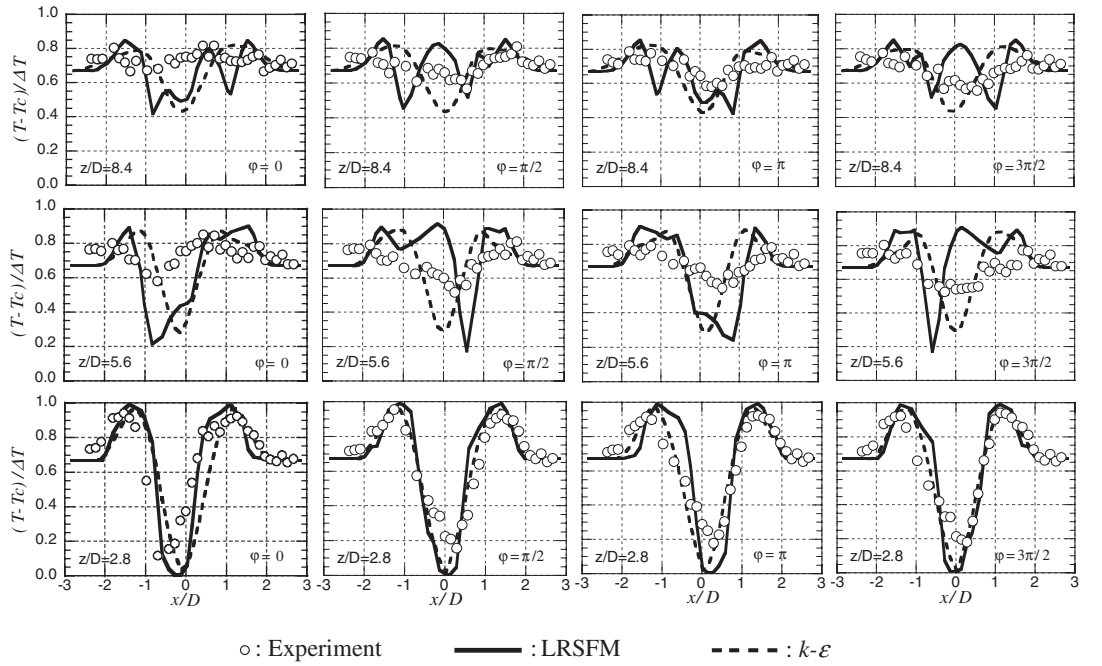

Figure 17. Comparisons of phase averaged temperature profiles.

jet, H, are used. The experimental points were acquired by UVP and shows data containing scattered noise beyond $x/H > 1$, at the right. The LRSFM agrees well with the experiment, while the k–ε model predicts a flatter profile around the centreline.

Lastly, profiles of the phase-averaged temperature, $T + \tilde{t}$, are presented in Figure 17. Details are presented in Reference [31] on the phase averaging method applied to the experiment. Both prediction results are not satisfactory with respect to agreement with the experiment. The k–ε model consistently shows stable profiles of the phase-averaged temperature such that the profiles are nearly symmetrical and the axis of symmetry stays around the centreline of the cold jet. As for the LRSFM, the predicted result exhibits significant variation of the phase-averaged temperature profile. At certain positions and phase angles, the LRSFM and the experiment agree qualitatively. As seen in Figure 10, the LRSFM over-predicted the coherent oscillation, $\tilde{t}$; that is, it under-predicted the random component of temperature fluctuation, t'. On the other hand, the experimental result contains a random fluctuation component produced by large-scale recirculating vortices beside the triple-jet, inside the plenum in which the jets are submerged. The contribution of large-scale vortices is not simulated in the present computations. This could be one of the reasons for the difference between the LRSFM and the experiment.

Finally, with respect to proper numerical simulation of multiple, thermal jets, two physical mechanisms are thought to contribute to the accurate simulation of thermal mixing, these being: (1) a low level of turbulence (i.e. eddy viscosity) that induces the transverse oscillation of the jets thus enhancing mixing, and (2) substantial turbulent mixing downstream of the oscillation dominated region.

5. CONCLUDING REMARKS

The LRSFM were presented with the algebraic function for the wall boundary condition of ε. The latter is to improve the model capability on a coarse meshes for practical use. The results from validation studies showed that the present model is capable of predicting turbulent–laminar transition resulting from strong heating as well as the transition by change of Reynolds number. Moreover, the coarse meshes are applicable to the present model. Typical mesh width applied was 5 times or larger as compared to that used with the existing wall boundary condition for ε. The results from the predictions with the coarse meshes agreed with the accepted correlations for heat transfer and friction factor within the range: $Re < 5 \times 10^4$, $0.0044 < Pr < 10$. When the fine mesh was applied, the present model gave good agreement to Sleicher–Rouse [23] correlation up to $Pr = 10^3$. The present model thus enhances computational capability of the low Reynolds number second moment closure turbulence model. Namely applicability of the complex turbulence model to complicated phenomena is extended as compared to existing models.

URANS simulations using the LRSFM and the standard k–ε model were compared to an experiment with three vertical jets, the cold in between two hot jets, simulating the thermal mixing and temperature fluctuations anticipated at the outlet of a liquid metal fast reactor core.

The LRSFM could simulate the experimental results such as the oscillatory motion and mean profiles of the flow pattern. In fact, the LRSFM simulation indicated that the influence of turbulence on the thermal mixing was of second-order importance in contrast to the contribution by coherent phenomena that significantly contributed to the mixing via periodic oscillation of the jets. In particular, the periodic oscillation was most evident in the region where the three jets merged to form a composite jet. The LRSFM, however, over-predicted the variation of the phase-averaged temperature profiles.

In comparison, the k–ε model consistently under-predicted the mixing effect due to the oscillatory motion, such that a transverse mean temperature difference existed far downstream. Equally, a higher intensity of temperature fluctuation remained as compared to the experiment. We attributed this to the apparently high turbulent viscosity along the edge of the jets, thus constraining them from oscillating in the transverse direction. This prevented substantial thermal mixing.

APPENDIX A

Conservation equations for the LRSFM

Conservation of mass

$$\frac{\mathrm{D}\rho}{\mathrm{D}t} = 0 \tag{A1}$$

Momentum equations

$$\frac{\mathrm{D}\rho U_i}{\mathrm{D}t} = -\frac{\partial P}{\partial x_i} + \frac{\partial}{\partial x_j}\left(\mu \frac{\partial U_i}{\partial x_j} - \rho\overline{u_i' u_j'}\right) + g_i(\rho - \rho_0) \tag{A2}$$

Energy equations

$$\frac{\mathrm{D}\rho\bar{h}}{\mathrm{D}t} = \frac{\partial}{\partial x_i}\left(\frac{\lambda}{c_p}\frac{\partial \bar{h}}{\partial x_i} - \rho\overline{u_i' h'}\right) \tag{A3}$$

Reynolds stress equations

$$\frac{\mathrm{D}\rho\overline{u_i' u_j'}}{\mathrm{D}t} - \mathrm{DIFF}(\rho\overline{u_i' u_j'}) = P_{ij} + G_{ij} + \Phi_{ij} - \rho\varepsilon_{ij} \tag{A4}$$

Turbulence heat flux equations

$$\frac{\mathrm{D}\rho\overline{u_i' h'}}{\mathrm{D}t} - \mathrm{DIFF}(\rho\overline{u_i' h'}) = P_{it1} + P_{it2} + G_{it} + \Phi_{it} - \rho\varepsilon_{it} \tag{A5}$$

Energy fluctuation equation

$$\frac{\mathrm{D}\rho\overline{h' h'}}{\mathrm{D}t} - \mathrm{DIFF}(\rho\overline{h' h'}) = P_h - 2\rho\varepsilon_h \tag{A6}$$

Equation of turbulent kinetic energy dissipation rate

$$\frac{\mathrm{D}\rho\varepsilon}{\mathrm{D}t} - \mathrm{DIFF}(\rho\varepsilon) = (C_{1\varepsilon} + \varphi_1 + \varphi_2)\frac{\varepsilon}{k}P_k + C_{3\varepsilon}\frac{\varepsilon}{k}G_k - C_{2\varepsilon}\frac{\rho\varepsilon\tilde{\varepsilon}}{k} \tag{A7}$$

$$\tilde{\varepsilon} = \varepsilon - 2\nu\left(\frac{\partial k^{1/2}}{\partial x_n}\right)^2 \tag{A7a}$$

where
Substantial derivative

$$\frac{\mathrm{D}}{\mathrm{D}t} = \frac{\partial}{\partial t} + U_j\frac{\partial}{\partial x_j} \tag{A8}$$

Diffusion terms

$$\mathrm{DIFF}(\rho\overline{u_i' u_j'}) = \frac{\partial}{\partial x_k}\left\{\left(\mu\delta_{kl} + C_s\frac{k}{\varepsilon}\rho\overline{u_k' u_l'}\right)\frac{\partial\overline{u_i' u_j'}}{\partial x_l}\right\} \tag{A9}$$

$$\mathrm{DIFF}(\rho\overline{u_i' h'}) = \frac{\partial}{\partial x_k}\left[\left\{\left(\frac{\mu}{2} + \frac{\lambda}{2c_p}\right)\delta_{kl} + C_{ht}\frac{k}{\varepsilon}\rho\overline{u_k' u_l'}\right\}\frac{\partial\overline{u_i' h'}}{\partial x_l}\right] \tag{A10}$$

$$\mathrm{DIFF}(\rho\overline{h' h'}) = \frac{\partial}{\partial x_k}\left\{\left(\frac{\lambda}{c_p}\delta_{kl} + C_{hr}\frac{k}{\varepsilon}\rho\overline{u_k' u_l'}\right)\frac{\partial\overline{h' h'}}{\partial x_l}\right\} \tag{A11}$$

$$\mathrm{DIFF}(\rho\varepsilon) = \frac{\partial}{\partial x_k}\left\{\left(\mu\delta_{kl} + C_{s\varepsilon}\frac{k}{\varepsilon}\rho\overline{u_k' u_l'}\right)\frac{\partial\varepsilon}{\partial x_l}\right\} \tag{A12}$$

Production terms

$$P_{ij} = -\left(\rho\overline{u_i'u_k'}\,\frac{\partial U_j}{\partial x_k} + \rho\overline{u_j'u_k'}\,\frac{\partial U_i}{\partial x_k}\right) \tag{A13}$$

$$P_{it1} = -\rho\overline{u_i'u_k'}\,\frac{\partial \bar{h}}{\partial x_k} \tag{A14}$$

$$P_{it2} = -\rho\overline{u_k'h'}\,\frac{\partial U_i}{\partial x_k} \tag{A15}$$

$$P_h = -2\rho\overline{u_i'h'}\,\frac{\partial \bar{h}}{\partial x_i} \tag{A16}$$

$$P_k = -\rho\overline{u_i'u_k'}\,\frac{\partial U_i}{\partial x_k} \tag{A17}$$

$$G_{ij} = -\frac{\rho}{c_p}\,\beta(g_i\overline{u_j'h'} + g_j\overline{u_i'h'}) \tag{A18}$$

$$G_{it} = -\frac{\rho}{c_p}\,\beta g_i\overline{h'h'} \tag{A19}$$

$$G_k = -\frac{\rho}{c_p}\,\beta g_i\overline{u_i'h'} \tag{A20}$$

Pressure strain terms

$$\Phi_{ij} = \Phi_{ij1} + \Phi_{ij2} + \Phi_{ij3} + \Phi_{ijw} \tag{A21}$$

$$\Phi_{ij1} = -C_1\,\frac{\rho\varepsilon}{k}\left(\overline{u_i'u_j'} - \frac{2}{3}\,\delta_{ij}k\right) \tag{A22}$$

$$\Phi_{ij2} = -C_2\left(P_{ij} - \frac{2}{3}\,\delta_{ij}P_k\right) \tag{A23}$$

$$\Phi_{ij3} = -C_3\left(G_{ij} - \frac{2}{3}\,\delta_{ij}G_k\right) \tag{A24}$$

$$\begin{aligned}\Phi_{ijw} = \Bigg\{ & C_1'\,\frac{\rho\varepsilon}{k}\left(\overline{u_k'u_m'}n_kn_m\delta_{ij} - \frac{3}{2}\,\overline{u_k'u_i'}n_kn_j - \frac{3}{2}\,\overline{u_k'u_j'}n_kn_i\right) \\ & + C_2'\left(\Phi_{km2}n_kn_m\delta_{ij} - \frac{3}{2}\,\Phi_{ik2}n_kn_j - \frac{3}{2}\,\Phi_{jk2}n_kn_i\right) \\ & + C_3'\left(\Phi_{km3}n_kn_m\delta_{ij} - \frac{3}{2}\,\Phi_{ik3}n_kn_j - \frac{3}{2}\,\Phi_{jk3}n_kn_i\right)\Bigg\}\,\frac{k^{3/2}}{C_l\varepsilon x_n}\end{aligned} \tag{A25}$$

where x_n is the distance from a wall and n_i the unit vector in the x_n direction.

Pressure temperature fluctuation gradient correlation terms

$$\Phi_{it} = \Phi_{it1} + \Phi_{it2} + \Phi_{it3} + \Phi_{itw} \tag{A26}$$

$$\Phi_{it1} = -C_{t1}\frac{\rho\varepsilon}{k}\overline{u_i'h'} - C_{t1n}\frac{\rho\varepsilon}{k}a_{ij}\overline{u_j'h'} \tag{A27}$$

$$\Phi_{it2} = -C_{t2}(P_{it1} + P_{it2}) \tag{A28}$$

$$\Phi_{it3} = -C_{t3}G_{it} \tag{A29}$$

$$\Phi_{itw} = C_{t1}'\Phi_{kt1}n_k n_i \frac{k^{3/2}}{C_l\varepsilon x_n} \tag{A30}$$

Dissipation rate

$$\varepsilon_{ij} = \frac{2}{3}\delta_{ij}\varepsilon \tag{A31}$$

$$\varepsilon_{it} = 0 \tag{A32}$$

$$\varepsilon_h = C_{h1}\frac{\overline{h'h'}}{k}\varepsilon \tag{A33}$$

Functions for the low Reynolds number treatment

$$\varphi_1 = C_{\varphi1}A(P_k/\varepsilon - 1.0) \tag{A34a}$$

$$C_{\varphi1} := 1.5 \tag{A34b}$$

$$\varphi_2 = C_{\varphi2}(1 - 0.3A_2)\exp\{-(0.002R_T)^{1/2}\} \tag{A35a}$$

$$C_{\varphi2} := 0.35 \tag{A35b}$$

$$C_1 = 1 + 2.58AA_2^{1/4}[1 - \exp\{-(0.0067R_T)^2\}] \tag{A36}$$

$$C_2 = 0.75A^{1/2} \tag{A37}$$

$$C_1' = -2C_1/3 + 1.67 \tag{A38}$$

$$C_2' = \max[2(C_2 - 1)/3 + 0.5, 0]/C_2 \tag{A39}$$

$$A = 1 - \frac{9}{8}(A_2 - A_3) \tag{A40}$$

$$A_2 = a_{ij}a_{ji} \tag{A41}$$

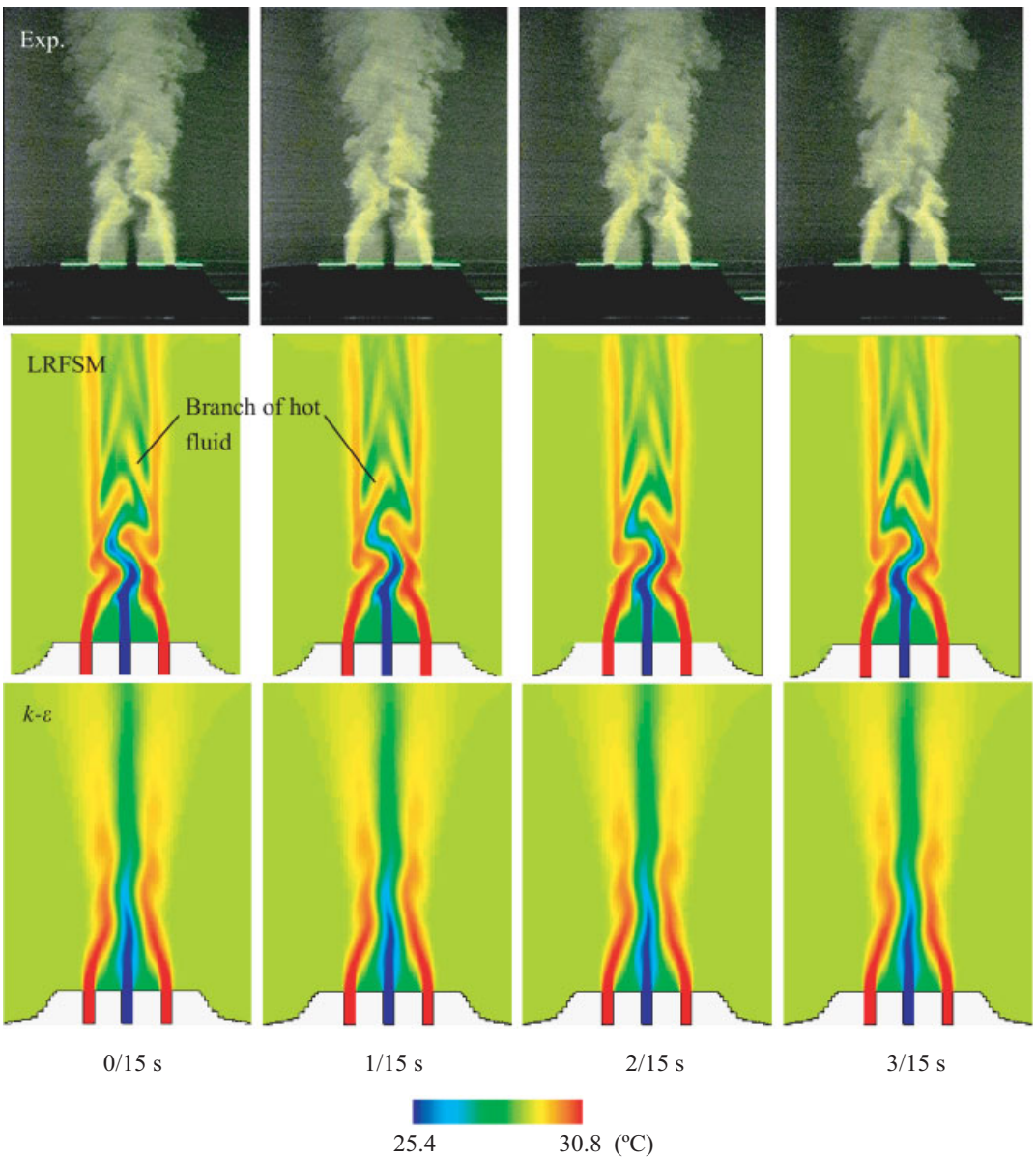

Plate 1. Instantaneous flow fields and predicted contour of iso-therms.

$$A_3 = a_{ij}a_{jk}a_{ki} \tag{A42}$$

$$a_{ij} = \frac{\overline{u_i u_j}}{k} - \frac{2}{3}\delta_{ij} \tag{A43}$$

$$R_T = \frac{k^2}{\nu\varepsilon} \tag{A44}$$

Empirical constants are shown in Tables A1–A3.

Table A1. Empirical constants for Reynolds stress equations.

C_s	C_1	C_2	C_3	C_1'	C_2'	C_3'	C_l
0.22	Eq.(A36)	Eq.(A37)	0.6	Eq.(A38)	Eq.(A39)	0.0	2.5

Table A2. Empirical constants for turbulence heat flux and energy fluctuation equations.

C_{ht}	C_{t1}	C_{t1n}	C_{t2}	C_{t3}	C_{t1}'	C_{hr}	C_{h1}
0.15	4.5	2.2	0.4	0.33	0.25	C_s	0.62

Table A3. Empirical constants for ε equation.

$C_{s\varepsilon}$	$C_{1\varepsilon}$	$C_{2\varepsilon}$	$C_{3\varepsilon}$
0.18	1.44	1.92	0.7

APPENDIX B: NOMENCLATURE

c_p specific heat at constant pressure, J/kg/K
D hydraulic diameter, m
G mean mass flux, $\dot{m}/(0.25\pi D^2)$, kg/(m^2 s)
h instantaneous specific enthalpy, i.e. enthalpy per unit mass, J/kg
H half-width of a jet, m
k turbulent kinetic energy, m^2/s^2
$\dot{m}$ mass flow rate, kg/s
q''_{w} wall heat flux, W/m^2
t instantaneous temperature (°C), time s
T time-mean temperature, °C
U time-mean axial and transverse velocity components for the flow in the tube and the triple-jet, respectively, m/s

W time-mean vertical velocity component, m/s
u instantaneous axial and transverse velocity components for the flow in the tube and the triple-jet, respectively, instant velocity component in the direction notified by subscript i, j or k, m/s
u_τ friction velocity $= \sqrt{\tau_w/\rho}$, m/s
v instantaneous spanwise velocity component, m/s
x axial co-ordinate for the flows in the tubes, transverse co-ordinate with the origin at the centreline of the centre jet for the triple-jets, m
x_n, y co-ordinate perpendicular to the wall with the origin on the wall, m
z vertical position, measured from the outlet of the jet nozzle, m

Non-dimensional quantities

Gr Grashof number $= g\beta\Delta T D^3/\nu^2$
Pr Prandtl number
q^+ heat flux, $q''_w/Gc_p\Theta$; q_i^+, based on inlet conditions, $q''_w/Gc_{pin}\Theta_{in}$
Re inlet or bulk Reynolds number $= (U_{in}$ or $U_b)D/\nu$
Re_τ Reynolds number based on the friction velocity $= u_\tau\delta/\nu$
Ri Richardson number $= Gr/Re^2$
y^+ non-dimensional distance from the wall $= u_\tau y/\nu$

Greek letters

ΔT injection temperature difference $= T_h - T_c$, °C
ε dissipation rate of turbulent kinetic energy, m^2/s^3
Θ absolute temperature, °K
φ phase angle, rad
λ thermal conductivity, W/m/°C
μ absolute viscosity, Pa s
ν kinematic viscosity, m^2/s
ρ specific weight of fluid, kg/m^3
τ shear stress, Pa

Subscripts

b bulk
c variable concerning cold jet
exp experiment. For the non-dimensional quantities Gr_{exp}, Re_{exp} and Ri_{exp}, ΔT and D correspond to temperature difference between the hot and cold jets and slit nozzle hydraulic diameter, respectively
h variable concerning hot jets
i or in inlet
LMFR liquid metal fast reactor. For the non-dimensional quantities Gr_{LMFR}, Re_{LMFR} and Ri_{LMFR}, ΔT is about 100°C, temperature difference between the fuel and control rod subassemblies, and D typically about 100 mm, diameter of an outlet nozzle of the subassemblies

m maximum value in the cross-section under consideration
RMS root mean square value
w wall

Superscripts

′ fluctuation component due to turbulence, e.g. $u' = u - U$

Miscellaneous

Overbar time-mean quantity
∼ coherent component of a fluctuation

ACKNOWLEDGEMENTS

The authors are grateful to Professor D.M. McEligot of Idaho National Engineering and Environmental Laboratory and the University of Arizona, Professor A. Tokuhiro of university of Missouri-Rolla, Dr I. Maekawa and Dr S. Fujii of Kawasaki Heavy Industries Ltd. for their technical advice. The authors also acknowledge the contribution of Mr Y. Miyake of NDD Co. in performing the calculations and to the technicians of Joyo Sangyo Co. for their technical and engineering support of the experiments.

REFERENCES

1. Tucker PG, Pan Z. URANS computations for a complex internal isothermal flow. *Computational Method in Applied Mechanics and Engineering* 2001; **190**:2893–2907.
2. Tatsumi K, Iwai H, Inaoka K, Suzuki K. Flow and heat transfer characteristics on turbulent flows in a duct with rib turbulators. *Proceedings of the 3rd International Symposium On Turbulence*, *Heat and Mass Transfer* (*THMT*-3), Nagoya, Japan, 2000; 207–214.
3. Maekawa I. Numerical diffusion in single-phase multi-dimensional thermal-hydraulic analysis. *Nuclear Engineering and Design* 1990; **120**:323–339.
4. Kimura N, Tokuhiro A, Miyakoshi H. An experimental investigation on thermal striping. Part I: Mixing of a vertical cooled jet with two adjacent heated jets as measured by ultrasound Doppler velocimetry. Part II: Heat transfer and temperature measurement results. *Proceedings of the 8th International Topical Management on Nuclear Reactor Thermal Hydraulics* (*NURETH*-8), Kyoto, Japan, vol. 3, 1997; 1712–1734.
5. Tokuhiro A, Kimura N. An experimental investigation on thermal striping mixing phenomena of a vertical non-buoyant jet with two adjacent buoyant jets as measured by ultrasound Doppler velocimetry. *Nuclear Engineering and Design* 1999; **188**:49–73.
6. *Ultrasound Velocity Profile monitor*, *Model X-1*, *Met-Flow SA*. Lausanne, Switzerland, 1992.
7. Takeda Y. Instantaneous velocity profile measurement by ultrasonic Doppler method. *JSME International Journal* 1995; **38**:8–16.
8. Nishimura M, Tokuhiro A, Kimura N, Kammide H. Numerical study on mixing of oscillating quasi-planar jets with low Reynolds number turbulent stress and heat flux equation models. *Nuclear Engineering and Design* 2000; **202**:77–95.
9. Nishimura M. Development of a low Reynolds number turbulence stress and heat flux equation model (A new type wall boundary condition for dissipation rate of turbulent kinetic energy aided by DNS data base) *JNC Report*, O-arai engineering Center, PNC TN9410 98-027, 1998 (in Japanese).
10. Shima N. A Reynolds stress model incorporating the effect of high anisotropy (1st report, modeling and application to a flat plate boundary layer). *Transactions of the Japan Society of Mechanical Engineers* 1988; **54**(505):2317–2324 (in Japanese).
11. Shima N. Calculation of turbulent boundary layers with transpiration using a second-moment closure. *Transactions of the Japan Society of Mechanical Engineers* 1989; **55**(515):1904–1910 (in Japanese).
12. Shima N. Calculation of rotating channel flow using Reynolds stress model. *Transactions of the Japan Society of Mechanical Engineers* 1989; **55**(516):2198–2204 (in Japanese).
13. Shima N. Prediction of a three-dimensional turbulent boundary layer on a swept wing. *Transactions of the Japan Society of Mechanical Engineers* 1991; **57**(534):419–426 (in Japanese).

14. Launder BE. Heat and mass transport. In *Topics in Applied Physics*: *Turbulence*, Bradshaw P (ed.), vol. 12. Springer: Berlin, 1976; 231–287.
15. Nishimura M, Fujii S, Shehata AM, Kunugi T, McEligot DM. Prediction of forced gas flows in circular tubes at high heat fluxes accompanied by laminarization. *Journal of Nuclear Science and Technology* 2000; **37**:581–894.
16. Yang Z, Shih TH. A Galliean and tensorial invariant k–ε model for near wall turbulence. *Proceedings of the AIAA 24th Fluid Dynamic Conference*, Orlando, 1993; AIAA-93-3105.
17. Khalil EE, Spalding DB, Whitelaw HH. The calculation of local flow properties in two-dimensional furnaces. *International Journal of Heat and Mass Transfer* 1975; **18**:775–791.
18. Kuroda A, Kasagi K, Hirata M. Investigation of dynamic effects of the mean shear rate on the wall turbulence via direct numerical simulation. *Data Base on Turbulent Heat Transfer of Japan Society of Mechanical Engineers* 1997; URL, http://ted.mech.titech.ac.jp/HTDB/dathetj.html.
19. Kawamura H. *DNS database of Turbulent Channel Flow*, 2000; URL, http://muraibm.me.noda.sut.ac.jp/homepage/e-database1.html.
20. Nishimura M. Development of a low Reynolds number turbulence stress and heat flux equation model. *Proceedings of the 7th International Conference on Nuclear Engineering* (*ICONE-7*), Tokyo, Japan, 1999, CD-ROM.
21. McEligot DM, Ormand LW, Perkins HC. Internal low Reynolds number turbulent and transitional gas flow with heat transfer. *Journal of Heat Transfer* 1966; **88**:239–245.
22. Kirillov PL, Subbotin VI, Ushakov PA. *Zhidkiye Metally* (*Liquid Metals*). Atomizdat: Moscow USSR, 1967.
23. Sleicher CA, Rouse MW. A convenient correlation for heat transfer to constant and variable property fluids in turbulent pipe flow. *International Journal of Heat and Mass Transfer* 1975; **18**:677–683.
24. Dittus FW, Boelter LMK. Heat transfer in automobile radiators of the tubular type. *Pub. in Engrg.*, vol. 2, University of California, 1930; 443–461.
25. Shehata AM. Mean turbulence structure in strongly heated air flows. *Ph.D. Thesis*, University of Arizona, 1984.
26. Fujii S, Akino N, Hishida M, Kawamura H, Sanokawa K. Experimental and theoretical investigations on heat transfer of strongly heated turbulent gas flow in an annular duct. *JSME International Journal Series II* 1991; **34**(3):348–354.
27. Hallbäck M, Johansson AV, Burden D. The basics of turbulence modeling, in Turbulence and Transition Modeling. In *Lecture Notes from the ERCOFTAC/IUTAM Summer School held in* Stockholm, 12–20 June, 1995, Hallback M, Henningson DS, Johansson AV, Alfredson PH (eds). Kluwer Academic Publishers: Dordrecht, 1996; 105.
28. Domanus HM. A new implicit numerical solution scheme in the COMMIX-1A computer program. *ANL 83-64*, *NUREG/CR-3435*, 1983.
29. Reynolds WC, Hussain AKMF. The mechanics of an organized wave in turbulent shear flow. Part 3. Theoretical models and comparisons with experiments. *Journal of Fluid Mechanics* 1972; **54**(part 2):263–288.
30. Hussain AKMF. Coherent structures—reality and myth. *Physics of Fluids* 1983; **26**:2816–2850.
31. Kimura N, Igarashi M, Kamide H. Investigation on convective mixing of triple-jet—evaluation of turbulence quantities using particle image velocimetry and direct numerical simulation. *Proceedings of the 8th International Symposium on Flow Modeling and Turbulence Measurements* (*FMTM2001*), Tokyo, 2001; CD-ROM.

